A spatial reconstruction of Siberian Last Glacial Maximum climate from pollen data

Nils Weitzel[1], Andreas Hense[2], Ulrike Herzschuh[3,4,5], Thomas Böhmer[3], Xianyong Cao[3,6], Kira Rehfeld[1]

[1] Institute of Environmental Physics, Heidelberg University, Heidelberg, Germany

[2] Institute of Geosciences, Sect. Meteorology, University Bonn, Bonn, Germany

[3] Alfred-Wegener-Institut Helmholtz-Zentrum für Polar- und Meeresforschung, Research Unit Potsdam, Potsdam, Germany

[4] Institute of Environmental Sciences and Geography, University of Potsdam, Potsdam, Germany

[5] Institute of Biochemistry and Biology, University of Potsdam, Potsdam, Germany

[6] Key Laboratory of Alpine Ecology, CAS Center for Excellence in Tibetan Plateau Earth Sciences, Institute of Tibetan Plateau Research, Chinese Academy of Sciences, Beijing, China

Correspondence: Nils Weitzel (nweitzel@iup.uni-heidelberg.de)

The Last Glacial Maximum (LGM, around 21.000 years before present) was a period with significantly colder global mean temperature, large Northern Hemisphere ice sheets, and lower CO_2 concentrations. Siberia was affected by a lower sea level which led to a closed Bering strait and a northward shift of the Arctic Ocean coastline. However, unlike other high-latitude areas, Siberia was not covered by a terrestrial ice sheet at that time. Climate simulations with LGM boundary conditions show large inter-model differences especially in Northern Siberia, which impede a direct analysis of Siberian LGM climate from simulations. Preserved pollen samples provide information on the LGM vegetation and climate state.

We reconstruct mean temperature of the warmest month and mean annual precipitation from a network of pollen samples using weighted averaging partial least squares transfer functions. Combining these local reconstructions with a multi-model ensemble of PMIP3 climate simulations in a Bayesian framework, we obtain the first probabilistic spatial reconstruction of Siberian LGM climate. Our reconstruction shows less cold summer temperature anomalies along the coastlines than in Western Siberia, and a weaker precipitation reduction in Eastern Siberia compared to Western Siberia. Finally, we quantify the mismatch between each ensemble member and the proxy data. By examining common features among similarly performing simulations, we find that most simulations with a comparatively warm and wet Siberian climate score better.

Our data constrained state estimate is well-suited for future analyses of Siberian LGM climate. Potential applications include the investigation of reasons for the absence of a Siberian ice sheet during the LGM, the quantification of land-atmosphere carbon fluxes, and the estimation of past afforestation rates.

---

1 Introduction

During the Last Glacial Maximum (LGM), around 21.000 years before present (21ka), the global mean temperature was significantly colder than today. Large areas of the Northern Hemisphere, in particular

North America, Greenland, and Fennoscandia, were covered by ice sheets (Batchelor et al., 2019), the CO_2 concentration was at less than half of current values with around 185 ppm (Köhler et al., 2017), and the sea level was around 120 m below the present level (Lambeck et al., 2014). Overall, insolation was higher-than-preindustrial in winter in both hemispheres, and lower-than-preindustrial in summer in both hemispheres (Otto-Bliesner et al., 2006). This corresponds to a reduced seasonal contrast in the top-of-atmosphere radiation. Therefore, the LGM is an important period for studying the Earth system under a different background climate state and for evaluating climate models under boundary conditions that are far from present-day values (Kageyama et al., 2017).

We focus on the LGM state eastward from the Ural mountains (Fig. 1). Siberia is structured by the major rivers Ob, Jenissei, Lena and Kolyma. Our domain of interest extends to the Arctic Ocean in the north, the Pacific Ocean in the East, and south to the Gobi dessert. Major topographic features of this region are the lowlands between Ob and Jenissei (Western Siberia), medium elevation highlands between Jenissei and Lena (Central Siberia), highlands east of the Lena (Eastern Siberia / Western Beringia), and topographically complex highlands south of the Baikal Lake. Today, most of Siberia is exposed to a very continental climate due to dominant westerly winds, which lead to decreasing precipitation from 500 – 800 mm annual precipitation in Western Siberia to 100 – 400 mm annual precipitation in Eastern Siberia (Karger et al., 2017). Cold and dry winters facilitate the forming of a persistent Siberian high pressure system during winter (Gong and Ho, 2002), whereas a Siberian low is the dominant pressure system during summer. Mean July temperatures are as high as 20° C in southern Siberia but only around 10° C in the northernmost parts (Rohde et al., 2013). Only a small sector along the Pacific coast from the Bering strait via the Kamchatka peninsula and the Sea of Okhotsk to the Amur region is influenced more by easterly winds leading to higher precipitation rates with the Pacific as main moisture source (Mock et al., 1998).

As the Siberian shelf is mostly shallow, the lower sea levels at the LGM led to a closed Bering strait and a northward retreat of the Arctic Ocean by several hundreds of kilometers (shaded area in Fig. 1). However, unlike other high-latitude areas on the Northern Hemisphere, Siberia was not covered by a large terrestrial ice sheet during the LGM. Only the most northwestern part of our domain of interest was covered by the tails of the Barents-Kara ice sheet (Fig. 1, Hughes et al., 2015; Abe-Ouchi et al., 2015). The maximum Siberian glacier extent was probably reached around 90ka (Hughes et al., 2013), followed by a subsequent glacier retreat in connection with increased Fennoscandian glaciation, which was only interrupted by a minor glacial advance around 50ka (Svendsen et al., 2004; Stauch and Gualtieri, 2008). In the Pacific sector glaciers were near present-day extension during the LGM (Meyer and Barr, 2017; Stauch and Gualtieri, 2008).

Information on Siberian climatic conditions during the LGM are available from pollen samples (e.g. Tarasov et al., 1999), macrofossils (e.g. Kienast et al., 2005), faunal remains (e.g. Sher et al., 2005), boreholes (e.g. Dorofeeva et al., 2002), stable isotopes in ice wedges (e.g. Meyer et al., 2002), and diatoms and biogenic silica (e.g. Colman et al., 1995). Among these, pollen records have the highest spatial coverage.

For Western Siberia, pollen-based reconstructions from Tarasov et al. (1999) show substantially reduced precipitation during the LGM and colder summer temperature anomalies in mid-latitudes than in high latitudes. The Baikal lake is well studied from lake sediment records (Colman et al., 1995; Williams et al., 1997). Climate changes are mostly inferred from diatoms and biogenic silica but quantitative climate reconstructions are not available. Borehole temperature reconstructions show minimal glacial temperatures with mean annual temperature anomalies of -10 K around 90ka (Dorofeeva et al., 2002), coinciding with the maximal Siberian glacier extent. Subsequent warming leads to an LGM anomaly of around -4 K compared to present-day.

In high-latitude Central Siberia and along the Arctic Ocean coastline, dryer conditions than today are reconstructed from a variety of proxies (e.g. Sher et al., 2005; Pitul'Ko et al., 2007; Andreev et al., 2011; Ashastina et al., 2018; Opel et al., 2019). Stable isotope analyses and macrofossils indicate regionally homogeneous colder winter temperatures (e.g. Meyer et al., 2002; Kienast et al., 2005; Andreev et al., 2011; Wetterich et al., 2011; Opel et al., 2019). In contrast, inconsistent results are reported for summer temperature. While Andreev et al. (2011) deduce colder-than-present summers from pollen and insect assemblages along the Arctic Ocean coastline, Kienast et al. (2005) and Sher et al. (2005) interpret macrofossil, insect, and mammal findings from the Lena delta as indicators of warmer or similar to present-day summer temperatures. Pitul'Ko et al. (2007) and Ashastina et al. (2018) infer slightly cooler LGM summer temperatures from pollen records in the Yana region between Lena and Kolyma.

In Eastern Siberia, Berman et al. (2011) reconstruct positive LGM summer temperature anomalies for the Kolyma region from invertebrates. Within uncertainties, this range coincides with similar to present-day summer temperature estimates by Alfimov and Berman (2001). In the same study, strongly positive anomalies are reconstructed for Ayon Island, which was part of the Siberian mainland during the LGM. In contrast, Lozhkin et al. (2007) reconstruct substantially negative summer temperature anomalies for the more continental El'gygytgyn Lake. In the Pacific sector, Meyer et al. (2017) reconstruct LGM summer temperatures similar to today on Kamchatka peninsula from branched glycerol dialkyl glycerol tetraethers and infer similar or higher precipitation amounts from these estimates via indirect glacier modeling (Meyer and Barr, 2017). Off the Pacific coast, Kiefer et al. (2001) and Meyer et al. (2016) infer summer sea surface temperature anomalies around -1.5 K from Foraminifera assemblages and Tetra Ether index (TEX_{86}) based paleothermometry in the Northwest Pacific, compared to -2 K to -6 K anomalies in MARGO Project Members (2009). For the Sea of Okhotsk, Seki et al. (2009) infer summer SST anomalies of -3 K from TEX_{86}.

Despite these efforts, Siberia is currently underrepresented in global climate reconstruction compilations (Bartlein et al., 2011) and no spatial reconstruction of the Siberian LGM climate exists to date. Climate model simulations of present-day conditions feature substantial surface temperature biases and inter-model differences over Siberia (Miao et al., 2014). As a consequence, large uncertainties persist in future temperature projections. Even larger inter-model differences exist for simulations of Siberian climate under LGM conditions (see Fig. 5 and Online Resource 1). To get a better constrained state estimate of LGM climate conditions and to quantify the ability of climate models to simulate the Siberian LGM climate, we extend the previously available spatial synthesis of proxy records.

Due to the absence of large ice sheets, fossil pollen samples from the LGM are preserved in lake sediments and peat bogs. We compile a synthesis of published pollen records covering large parts of Siberia. From this proxy network, we reconstruct mean temperature of the warmest month (MTWA) and mean annual precipitation ($\mathrm{P}_{\mathrm{ANN}}$) during the LGM using the weighted averaging partial least squares (WAPLS) algorithm, which is a well-established statistical pollen-climate transfer function (Birks et al., 2010).

The spatial distribution of our pollen sample network is too coarse to create gridded maps with simple statistical interpolation. Therefore, using Bayesian statistics, we combine the local reconstructions with a multi-model ensemble of climate simulations from the Paleoclimate Modelling Intercomparison Project Phase III (PMIP3, Braconnot et al., 2011, 2012) to compute a spatial reconstruction of Siberian LGM climate. Our results refine previous global-scale estimates by Annan and Hargreaves (2013), and provide the first dedicated spatial reconstruction of Siberian climate at the LGM. A closely related approach was used by Cleator et al. (2019) to reconstruct the European LGM climate. In the spatial reconstruction, the proxy data provides local climate information whereas the simulations control the spatial interpolation between the proxy records (Weitzel et al., 2019). The result is a spatially distributed probability distribution, based on which the most probable state can be estimated, and a quantification of the uncertainty related to the proxy-climate relationship and the spatial interpolation. The Bayesian reconstruction framework facilitates a quantification of the deviation of each ensemble member from the proxy data taking into account those two sources of uncertainty.

The structure of this study is as follows: In the next section, we present the pollen data and climate simulation ensemble. The statistical pollen-climate transfer functions, the spatial reconstruction framework, and the simulation evaluation procedure are described in Sect. 3. In Sect. 4, we present results from the local and spatial reconstructions as well as the simulation ensemble evaluation. Finally, we discuss potential implications for atmospheric processes governing the Siberian LGM climate, compare our results with previous work, and discuss potential applications and extensions of our results in Sect. 5. In Online Resource 1, we provide technical descriptions of the statistical algorithms, evaluations of the statistical methods, and additional figures.

2 Data

2.1 Pollen samples

For local climate reconstructions, we use a compilation of 37 pollen records, which are located between 69° E and 178° W and 42° N and 75° N. The locations of the cores are depicted by black dots in Fig. 1. For each core, the raw radiocarbon dates as well as pollen percentages had to be available to be included in the synthesis. Age models were recalculated with the Bayesian age model Bacon (Blaauw and Christen, 2011) following Cao et al. (2013). We use all samples with calibrated mean age between 19ka and 23ka. This leads to a total of 170 samples. The records are the LGM subset of a larger Siberian pollen compilation (Cao et al., 2020). The taxonomy of the pollen counts is homogenized as described in Cao et al. (2013), Cao et al. (2014), and Cao et al. (2020).

To apply statistical pollen-climate transfer functions, a modern pollen and climate calibration dataset is compiled, expanding the previously presented dataset for China and Mongolia (Cao et al., 2014). MTWA, mean temperature of the coldest month (MTCO), and growing degree days above 5° C (GDD5) climatologies are derived from the Berkeley Earth Surface Temperature dataset (Rohde et al., 2013) for the period 1951 to 1980. $\mathrm{P_{ANN}}$ and mean annual temperature ($\mathrm{T_{ANN}}$) are extracted from the CHELSA high resolution climatologies for the period 1979 – 2013 (Karger et al., 2017).

The data collection and processing of the samples is described in detail in Cao et al. (2020) for the fossil data and in Cao et al. (2014) for the calibration data. Further information on the proxy records are provided in Online Resource 1.

2.2 Climate simulations

A multi-model ensemble of climate simulations, which was created within PMIP3, is used for interpolation in the spatial reconstructions and evaluated against the paleoclimate data. The boundary conditions in the simulations were adjusted to the LGM, including changed orbital configurations, greenhouse gas concentrations, ice sheets, and topography (Braconnot et al., 2011). Here, we rely on simulations from the CCSM4, COSMOS-ASO, FGOALS-g2, GISS-E2-R, IPSL-CM5A-LR, MIROC-ESM, MPI-ESM-P, and MRI-CGCM3 models in the PMIP3 project. The simulations form a multi-model ensemble with common boundary conditions, i.e. they follow the same experiment protocol. The models were run until an equilibrium state was obtained (spin-up), after which simulations were continued and archived for at least 100 years.

We interpolate all simulations bilinearly to a common 2° by 2° grid. The climatological means for the respective reconstruction variables are extracted. This minimizes inter-annual to decadal variability, which is not resolved by our proxy compilation and follows the procedure of Annan and Hargreaves (2013). Anomalies with respect to the preindustrial simulations are computed. For $\mathrm{P_{ANN}}$, we use the relative anomalies from the modern values, since they are more comparable across space.

Further properties of the simulations are provided in Online Resource 1.

3 Methods

The workflow summary in Fig. 2 shows how the datasets described in the Sect. 2 and the estimated statistical parameters contribute to the local reconstructions, the spatial reconstructions, and the ensemble member evaluation.

3.1 Local reconstructions

Local reconstructions from each pollen sample are performed with WAPLS transfer functions (Ter Braak and Juggins, 1993; Ter Braak et al., 1993) following the methodology from Cao et al. (2014). WAPLS is a regression-based statistical transfer function that consists of two stages (Birks et al., 2010). First, the climate optimum of each taxa is estimated based on the modern calibration dataset. Second, the climate optima are weighted according to the pollen percentages in the fossil pollen sample to obtain a local climate reconstruction. Partial least squares regression is used to account for residual correlations in the training data not explained by the respective climate variable. Uncertainty estimates are calculated using the bootstrapped RMSEP from cross-validation of the modern calibration dataset (Juggins, 2017). Due to the absence of core top samples for several records, anomalies of the reconstructions are calculated with respect to the calibration climatology.

The pollen percentages are square-root transformed prior to computing the transfer functions. For each proxy record, modern samples within a 2000 km radius are used for calibration, in order to include a sufficient environmental gradient for resolving glacial-interglacial differences. The number of used WAPLS components is selected from a randomization t-test (Juggins and Birks, 2012; van der Voet, 1994). Depending on the test results either one or two components for each of the records are chosen.

Climate reconstructions from statistical transfer functions can be biased if the signal of a dominant environmental variable superimposes the reconstructed variable (Juggins, 2013; Rehfeld et al., 2016). Therefore, the selection of important reconstruction variables, which explain independent parts of the variability in the pollen data, needs to be examined statistically. We test the potential to reconstruct MTWA, MTCO, GDD5, $\mathrm{T}_{\mathrm{ANN}}$, and $\mathrm{P}_{\mathrm{ANN}}$ using the coefficient of determination between observed and predicted variables in the calibration data (R^2), the root mean square error of prediction in the calibration data (RMSEP), and the significance test of Telford and Birks (2011), which tests the significance of the explained variance in the fossil data against randomized transfer functions. In these tests, MTWA and $\mathrm{P}_{\mathrm{ANN}}$ perform best for the highest number of records. The performance of $\mathrm{P}_{\mathrm{ANN}}$ is less correlated with the different temperature variables, which indicates that it explains more independent variance from MTWA than the other temperature variables. Therefore, MTWA and $\mathrm{P}_{\mathrm{ANN}}$ are chosen for local reconstructions from the pollen samples. These choices are in accordance with previous interpretations of Siberian pollen records as recorders of summer temperature and aridity (e.g. Alfimov and Berman, 2001; Kienast et al., 2005; Sher et al., 2005; Wetterich et al., 2011; Ashastina et al., 2018).

Results from the evaluation of the transfer function models are provided in Online Resource 1.

3.2 Spatial reconstruction framework

The spatial reconstruction framework is adapted from Weitzel et al. (2019). The strategy is to use the climate simulation ensemble for spatial interpolation and structural extrapolation of the local climate reconstructions from the pollen samples. The ensemble spread provides an additional constraint on physically reasonable climate states, particularly in regions that are sparsely covered by proxy records.

Our strategy to combine the two sources of information is based on Bayesian statistics. This allows us to separately model the proxy-climate relationship, called data stage, and the spatial interpolation, which is called process stage. Moreover, the Bayesian framework provides a natural way to incorporate uncertainties from the local reconstructions and the climate simulation ensemble. The goal is to estimate the so-called posterior probability, which is the probability of the past climate C_p, interpolation parameters ϑ, and transfer function parameters θ, conditioned on the proxy data P:

$$\underbrace{\mathbb{P}\left(C_p, \theta, \vartheta \,|\, P\right)}_{\text{Posterior}} \propto \underbrace{\mathbb{P}\left(P \,|\, C_p, \theta\right)}_{\text{Data stage}} \; \underbrace{\mathbb{P}\left(C_p \,|\, \vartheta\right)}_{\text{Process stage}} \; \underbrace{\mathbb{P}\left(\theta\right) \, \mathbb{P}\left(\vartheta\right)}_{\text{Prior stage}}. \tag{1}$$

The prior stage in Eq. (1) contains weakly-informative prior distributions of the parameters θ and ϑ which are necessary to ensure that the posterior distribution is a valid probability distribution.

The data stage models the incorporation of the information from the local reconstructions using a Gaussian observation model. The best estimates from the transfer functions are employed as data and the bootstrapped RMSEPs are the standard deviations of each proxy sample. The samples are modeled as unbiased estimators of the climate anomaly in their respective grid boxes. They influence the spatial reconstruction in other grid boxes only through the spatial interpolation. As part of the transfer function uncertainty is shared among samples from the same record, for example uncertainties related to the modern calibration dataset, we introduce a correlation parameter which estimates the shared fraction of the uncertainty. As the WAPLS transfer functions do not provide information on the amount of the dependent uncertainties, this parameter is fitted in the spatial reconstruction framework.

We previously tested several strategies to formulate the process stage (Weitzel et al., 2019). Here, we employ the best performing model from Weitzel et al. (2019), which is a multivariate Gaussian distribution estimated from the simulation ensemble with additional parameters. Compared to a purely Gaussian formulation, these parameters allow a more flexible adjustment of the ensemble to the proxy data and they mitigate overconfidence originating from climate simulation inadequacies and the small number of ensemble members. The mean of the Gaussian distribution is given by a weighted mean of the ensemble members. The weights are estimated from the local reconstructions. This gives more importance to ensemble members that fit better to the proxy data. The spatial covariance matrix of the Gaussian distribution combines the empirical covariance matrix of the simulation ensemble with a reference correlation matrix for regularization. Due to the relatively coarse resolution of the simulations, the empirical covariance mainly provides physically motivated estimates of the large-scale spatial correlations and the range of physically reasonable climate states. The reference correlation matrix decays with distance and models the small-scale correlations.

We infer the posterior distribution using Markov chain Monte Carlo methods. A technical description of the spatial reconstruction framework is provided in Online Resource 1. As in Weitzel et al. (2019), the reconstructions of MTWA and $\mathrm{P}_{\mathrm{ANN}}$ are evaluated with pseudo-proxy experiments using the climate simulation ensemble as reference climatologies and with cross-validation experiments. Details of the evaluation methods and evaluation results are given in Online Resource 1.

3.3 Ensemble member evaluation

We use the Bayesian framework to additionally quantify the deviation of proxy data and ensemble members. This is achieved by computing the log-likelihood score (LLS) of the ensemble members given the proxy data P. The LLS is a proper score function for probabilistic predictions (Gneiting and Raftery, 2007) and is therefore well-suited for model evaluations under uncertainties. For a given ensemble member M_k, the LLS is given by

$$\begin{aligned}\log \mathbb{P}\left(M_k \,|\, P\right) \;\propto\; \log \int & \mathbb{P}\left(P \,|\, C_p, \theta\right)\, \mathbb{P}\left(C_p \,|\, M_k, \vartheta\right) \\ & \mathbb{P}\left(M_k\right)\, \mathbb{P}\left(\vartheta\right)\, \mathbb{P}\left(\theta\right)\, dC_p\, d\vartheta\, d\theta. \end{aligned} \tag{2}$$

The LLS is derived from the spatial framework by integrating out C_p to get a direct likelihood of an ensemble member given the proxy data. We choose a flat prior for M_k, which gives equal prior probability to every possible climate state. A technical description of the evaluation method is provided in Online Resource 1.

The model-data comparison allows us to cluster simulations according to their fit with the proxy data. This clustering is used in Sect. 5.1 to study potential changes in the atmospheric circulation which govern the reconstructed MTWA and $\mathrm{P}_{\mathrm{ANN}}$ anomalies.

4 Results

4.1 Local reconstructions

The local reconstructions are shown in Fig. 3 together with the uncertainty estimates from the bootstrapped RMSEP. The estimated LGM anomalies show mostly cooler conditions with less precipitation compared to present-day. The reconstructions exhibit heterogeneity on large and medium spatial scales. Examples for large scale differences are more negative MTWA anomalies in continental Siberia compared to the coastlines, and more precipitation reduction in Central Siberia (Record IDs 1, 2, 16, 22, 24, 25, 26, 30, 31) than along the Arctic Ocean (IDs 12, 14, 17, 19, 28). On medium scales, we find for example deviations between the colder Yana region (IDs 14, 22, 25) and the upper Kolyma region (IDs 6, 8, 9, 11, 15, 23, 29, 37), where MTWA anomalies are near present-day values, and between the wetter Amur region (IDs 3, 4, 5, 20, 21, 32, 35, 36) and the dryer upper Kolyma region. Within these regions, the anomalies are relatively consistent, which indicates more homogeneous estimates on small spatial scales.

Mean MTWA anomalies of up to 5 K cooler than present-day are reached in large parts of the domain, but less negative and in some grid boxes even positive anomalies are present near the modern coastlines of the Arctic and Pacific Oceans and in the upper Kolyma region. With standard deviations between 1.0 K and 2.2 K, the temperature uncertainties of the samples are relatively homogeneous in space. However, higher temporal sampling rates can reduce the uncertainty of the mean anomalies of pollen records.

For most samples, lower-than-present precipitation is reconstructed, with a maximum reduction by around 60%. A regionally consistent increase of precipitation is only inferred in the Amur region. The transfer function uncertainties are typically large with standard deviations between 9.8 and 47.8 percentage points (%p).

In records with high temporal sampling rates, we find mostly small inter-sample variations during the 19ka to 23ka time slice. This supports our assumption of a relatively stationary LGM climate within the defined time period.

4.2 Spatial reconstructions

The area weighted mean anomaly of the spatial MTWA reconstruction is -1.9 K (see Table 1) with a 90% credible interval (CI) of (-2.7 K, -1.2 K). This spatial average is the result of regional heterogeneity with most negative LGM anomalies up to -8 K over the Barents-Kara ice sheet in the northwestern corner of the domain, and anomalies around -5 K in the southwestern part of the domain and over the open Pacific Ocean. In contrast, temperatures near modern values are reconstructed along most of the modern coastlines of the Arctic and Pacific Ocean and at the Sea of Okhotsk. An up to +7 K warmer LGM MTWA is featured in Arctic Ocean regions that are below sea level today but were above sea level during the LGM (Fig. 4a). The maximal positive and negative anomalies in the spatial reconstruction are considerably higher than in the local reconstructions (Fig. 3) due to structural spatial extrapolation via the climates simulations. For example, temperatures are near the modern values or slightly warmer along the modern coastline of the Arctic Ocean in the local reconstructions. PMIP3 simulations with similar values along the modern coastline produce pronounced warmer summers over the Siberian shelf that is now below sea level. The negative anomalies in the southeastern and southwestern part of the domain are mostly significant on a 5% level. However, in the central and northern areas anomalies are only significantly negative in regions with strong proxy constraints like the highland between Lena and Kolyma and over the most-northwestern area which was covered by the Barents-Kara ice sheet during the LGM.

Uncertainties (grid box-wise 90% CIs, Fig. 4c) feature a strong northwest-to-southeast gradient with CI sizes down to 2 K in the southeastern part of the domain and up to 14 K at the northwestern modern coastline of the Arctic Ocean. This pattern is similar to the ensemble spread in the PMIP3 simulations, which differ most in Northern Siberia and particularly over the Siberian shelf. The uncertainty in the unconstrained PMIP3 ensemble is reduced most near proxy records, but also large-scale features are better constrained. On average, the grid box-wise uncertainty reduction from the unconstrained PMIP3 ensemble to the spatial reconstruction is 58.4%.

The effect of proxy data on the posterior distribution is demonstrated by comparing two 20° times 10° areas, one in the eastern and one in the western part of the domain (rectangles in Fig. 1). In both regions the posterior mean is warmer than the prior mean and the posterior distribution is more constrained than the prior (Fig. 5). However, more proxy records are located in and near the eastern subdomain. Therefore, the reduction of uncertainty is much larger for this region.

Spatially averaged, the mean P_{ANN} anomaly is negative with 26.2% less precipitation during the LGM (Table 1). The 90% CI of that estimate is (-30.8%, -21.4%). The most-negative anomalies with up to 50% less precipitation are reconstructed in the northwestern part of the domain. Precipitation amounts similar to present-day climate are found in the Amur region due to the relatively high P_{ANN} values in the local reconstructions. In all other regions, the mean P_{ANN} anomalies are between -15% and -40%. Despite the large uncertainties in the local reconstructions, the anomalies in the spatial reconstruction are significant ($p \leq 0.05$) in most areas besides the Amur region as a result of negative anomalies in all PMIP3 simulations (Fig. 4b).

The spatial average of the grid box-wise 90% CI sizes is 34.0 %p, which is just an 8.9% reduction of uncertainty compared to the unconstrained PMIP3 ensemble. At grid boxes with proxy data, the reduction of uncertainty is largest with 21.8%, but the proxy signals are not spread out in space substantially due to much weaker spatial correlations than in the MTWA reconstructions. The smallest uncertainties are found in the same regions than in the unconstrained PMIP3 ensemble. The grid box-wise uncertainties are mostly between 20 %p and 50 %p, but extreme values down to 10 %p and up to 150 %p are featured in some grid boxes (Fig. 4d).

Overall, the MTWA reconstruction is more strongly influenced by the proxy data due to comparatively stronger constraints from the local reconstructions. This leads to higher ensemble member weights for comparatively warm simulations and those with decreasing anomalies from northeast to southwest. On average, the posterior mean is 3.3 K warmer than the PMIP3 ensemble mean and it is warmer across almost the whole domain. The highest weights are placed on the MRI-CGCM3, the COSMOS-ASO, and the IPSL-CM5A-LR simulations, whereas GISS-E2-R and MIROC-ESM have the lowest weights (see Online Resource 1). On the other hand, the spatial structure of the P_{ANN} reconstruction is close to that of the ensemble mean. However, the mean anomaly is 4.6 percentage points wetter than the ensemble mean and highest weights are given to the two wettest models, MPI-ESM-P and IPSL-CM5A-LR. In contrast, the driest model, MIROC-ESM, has the lowest weight.

Looking at the spatial covariance estimates, we find larger spatial correlations for MTWA than for P_{ANN}. We quantify this by computing the posterior mean $1/e$-decorrelation length (in degrees longitude/latitude) across space from fitting a smoothing spline to all pairs of grid boxes. For MTWA, the mean decorrelation length is 31.8°, whereas it is only 6.8° for P_{ANN} (Table 1). This finding indicates that large-scale spatial structures are better constrained by the proxy data for MTWA than for P_{ANN}. In addition to the stronger proxy constraints for MTWA, the larger spatial correlations lead to the stronger uncertainty reduction from the unconstrained PMIP3 ensemble to the posterior distribution.

The correlation parameter, which estimates the fraction of the dependent part of the transfer function uncertainty between samples from the same sediment core, is determined from discrepancies between local reconstructions of nearby pollen cores and the assumption of a stationary climate during the LGM time slice. The posterior distribution of this correlation parameter is well constrained by the proxy data for both variables. It is concentrated between 0.89 and 0.93 for MTWA and between 0.76 and 0.84 for P_{ANN} (Table 1). This means that among samples from one pollen record only 10-20% of the transfer function uncertainty is independent. As Fig. 3 shows that the assumption of a stationary climate during the LGM is reasonable, it indicates that the majority of the uncertainty is related to shared error sources like the modern calibration.

4.3 Evaluation of simulation ensemble

Fig. 6a shows the LLS for the eight ensemble members. In addition, the LLS of the ensemble mean and of a weighted mean, with weights according to the likelihoods of each ensemble member, is provided. For MTWA, the MRI-CGCM3 has the highest score, followed by COSMOS-ASO and IPSL-CM5A-LR. The highest LLS for P_{ANN} are achieved by MPI-ESM-P and IPSL-CM5A-LR. The IPSL-CM5A-R is the only model in the top three for both climate variables, whereas MIROC-ESM and GISS-E2-R are the bottom two for both variables. Besides, there is little coherence in the order of the ensemble members between MTWA and P_{ANN} LLS.

We find that the ensemble mean scores better than the mean LLS of the simulations, but below the best ensemble members. In contrast, the weighted mean performs similar to the best ensemble members. This means that the ensemble mean overcomes some of the deficiencies of individual ensemble members, the large inter-model differences still lead to a worse fit than the best ensemble members and the weighted mean.

Looking further into the model fit for different subregions, Fig. 6b-i shows the MTWA fit for moving windows of size 22° times 10°. In most cases, models with consistently good regional fits are also performing well in the whole domain analysis (e.g. MRI-CGCM3, IPSL-CM5A-LR, and COSMOS-ASO). However, the overall LLS is not just the average of the local fits, but corrects for the non-uniform spatial distribution of proxy records and takes into account potential teleconnections. For example, the MTWA MPI-ESM-P climatology performs above average in most subregions (Fig. 6h), but below-average in the whole-domain LLS due mismatches in the large-scale structures. The subregion analysis for P_{ANN} is included in Online Resource 1.

5 Discussion

5.1 Potential implications for atmospheric processes

The physical processes that lead to the large-scale Siberian climate in the models, and that are assessed by the LLS, can be investigated further. Therefore, we compare model-data mismatches and large-scale circulation features in different simulations.

In general, simulations with less cold and fairly wet conditions in Siberia perform better (compare Fig. 6a and Fig. 7a). Examples are the highest MTWA LLS for the MRI-CGCM3, which features the least negative MTWA LGM anomalies, and the highest P_{ANN} LLS for the MPI-ESM-P, which exhibits the smallest precipitation decrease. Exceptions from these relationships can be mostly traced back to deviating teleconnection patterns between proxy samples and climate simulations such as overestimated spatial gradients between subdomains.

Whether Siberia is warmer and wetter in a specific simulation does not relate to the global T_{ANN} anomaly or the global P_{ANN} anomaly in the respective models (Fig. 7a,b). However, there is a strong concordance between Siberian T_{ANN} and MTWA, although the magnitude of negative MTWA anomalies is smaller in all models. The relative reduction of precipitation is much larger in Siberia than globally, but across the different models, the coherence of P_{ANN} and T_{ANN} changes in Siberia is weak. This indicates that the precipitation decrease is more related to dynamic properties or microphysics than to thermodynamic constraints.

The LLS is strongly influenced by large-scale features like the spatial mean anomalies and north-south as well as east-west gradients. Northern Hemisphere polar amplification (Masson-Delmotte et al., 2006) controls the change of the temperature gradient between the Arctic and the Tropics. Therefore, it is potentially an important proxy of some of these large-scale features, for example the latitudinal anomaly gradient. Fig. 7c shows the ratio of the mean anomaly between 70° N and 90° N and between 0° and 20° N at 500 hPa, 600 hPa, and 700 hPa. These levels are chosen because at this altitude estimates are less influenced by the different representation of orographic features in the climate models and therefore a better indicator of the atmospheric state. During July, polar amplification at 600 hPa varies in the eight models between 1.2 in MRI-CGCM3 and 3.4 in GISS-E2-R. The four models, which perform best in either MTWA or P_{ANN}, are those with the smallest polar amplification factors during July and annually. These models also feature more stable estimates across the different pressure levels.

As Siberian climate is strongly influenced by the structure of the polar jet stream and the large-scale pressure systems, we look at the wind speed and geopotential height anomalies at 250 hPa (Fig. 8). To summarize the differences between simulations with higher and lower LLS, we compare the ensemble mean anomalies and the anomalies of the LLS-weighted mean, with weights from the MTWA evaluation. Plots of the anomalies for all ensemble members are provided in Online Resource 1. Most models show a band-structure with increased 250 hPa LGM wind speeds in the mid-latitudes accompanied by decreased wind speed in the terrestrial high latitudes and subtropics. However, the magnitude of the dipole between increased wind speed in the mid-latitudes and decreased wind speed in the high latitudes varies across the models. Fig. 8a,b show that this gradient is shallower in the weighted mean, which is dominated by simulations with high LLS values, compared to the ensemble mean, where low scoring models contribute equally to the ensemble average. However, both averages feature a slight northward shift of the mean jet stream position. While the unweighted ensemble mean features a strong negative geopotential height anomaly (Fig. 8c), in particular over Europe and Eastern Siberia (i.e. a more pronounced Eastern Siberian low than in the preindustrial simulations), the anomaly magnitudes are much smaller in the weighted mean (Fig. 8d) with just a slight negative anomaly, which might be caused by the overall cooler LGM atmosphere.

Assuming that better fitting ensemble members produce more realistic large-scale atmospheric structures which govern the surface temperature and precipitation patterns, we can deduce that during the

LGM the jet stream position was slightly shifted northward with stronger wind speeds over the mid-latitudes and reduced wind speeds over high latitudes. However, the intensification of the jet stream and the changes of the pressure structure was less extreme than in several simulations. The deviating magnitude of geopotential height anomaly between eastern and western North Pacific in the weighted mean suggests a westward shift of the North Pacific High, which is also hypothesized by Meyer et al. (2017). This might lead to the transport of relatively warm and moist air masses to the Pacific coastline and thus a weaker reduction of precipitation and MTWA in the better fitting simulations. The assumption that near-surface skill of an ensemble member is positively correlated to upper troposphere skill has been tested with mixed results on inter-annual scales in the Twentieth Century Reanalysis (Compo et al., 2011). It is unclear how these results translate to longer timescales. Future research to test these relationships could focus on the consistency of our results with reconstructions of European and North American LGM climates.

The improved performance of models with small negative or even positive MTWA anomalies along the coastlines of the Arctic and Pacific Ocean (cf. Online Resource 1) indicates that in these models the local MTWA anomalies are more directly influenced by the changed local energy balance due to the lower sea level. This explanation would fit with the simulation of reduced cloudiness and thus increased short-wave radiation at the surface by Löfverström et al. (2014). In the models with substantial cold anomalies along the shorelines, these local changes might be superimposed by the large-scale negative LGM anomaly signal as diagnosed also from the more extreme geopotential height and wind speed anomaly anomalies.

5.2 Comparison with previous work

In this section, we compare our results with previous climate reconstructions for different parts of Siberia as well as sea surface temperature (SST) reconstructions for the Northwestern Pacific. We structure this comparison geographically by looking at Western Siberia and the Baikal region, the Arctic Ocean coastline, Eastern Siberia, and the Pacific sector. The comparison is summarized in Table 2.

Our reconstruction supports the finding of less negative MTWA anomalies in the high latitudes of Western Siberia (+2 K to -3 K by Tarasov et al., 1999) than in the mid-latitudes (-3 K and -8 K by Tarasov et al., 1999) Meanwhile, the coldest anomalies in Tarasov et al. (1999) are a little warmer than in Western Siberia in our reconstruction, where local anomalies below -6 K are unlikely ($p \leq 0.05$). The borehole-based T_{ANN} LGM anomaly of around -4 K from Dorofeeva et al. (2002) is colder than our estimate of -1.4 K for the Baikal region. However, considering the likely cooler T_{ANN} than MTWA anomalies as well as local heterogeneity and reconstruction uncertainties, this result is still in concordance with our estimates (-4.1 K to +1.7 K, Table 2).

The complex anomaly pattern of our reconstruction in Central Siberia and along the Arctic Ocean (local anomaly ranges between -3.7 K and +6.6 K, including uncertainty estimates) is reflected in previous work. In the Yana region, we reconstruct moderate but statistically significant ($p \leq 0.05$) negative LGM MTWA anomalies. This is in agreement with the estimates of Pitul'Ko et al. (2007) and Ashastina et al. (2018). While Andreev et al. (2011) reports colder summer temperatures along the Arctic Ocean, Kienast et al. (2005) and Sher et al. (2005) find warmer or just slightly cooler summer temperatures in the Lena Delta. While we reconstruct negative but insignificant anomalies for the Taymyr Peninsula, our estimates of similar MTWA values to present-day for the Lena delta support the latter results. It also indicates that the results of Kienast et al. (2005) might not just be the effect of studying sheltered habitats as was suggested previously (Wetterich et al., 2011).

For Eastern Siberia, reconstructed positive MTWA anomalies by Berman et al. (2011) for the Kolyma region, estimates between -4 K and +3 K by Alfimov and Berman (2001), and LGM summer temperatures similar to present-day on Kamchatka Peninsula inferred by Meyer et al. (2017), are within the uncertainty ranges of our reconstruction. The strongly positive anomaly for Ayon Island reconstructed by Alfimov and Berman (2001) supports our finding of a warmer Siberian shelf due to the lower sea level. While we find significant negative MTWA anomalies in the more continental parts of Eastern Siberia, our reconstruction does not support the very cold estimate from Lozhkin et al. (2007).

For the Northwest Pacific, the inferred summer SST anomalies of around -1.5 K by Kiefer et al. (2001)

and Meyer et al. (2016) are in good agreement with our estimate of -2.3 K (with local anomalies between -4.6 K and -0.1 K). Similar to MARGO Project Members (2009), our reconstruction features a northwest to southeast gradient, but our lowest anomalies stay above the -6 K in the coolest MARGO grid box. The estimate of -3 K summer SST anomaly for the Sea of Okhotsk by Seki et al. (2009) is slightly cooler than our estimates. That the latter two estimates are more extreme than our results might be due to the higher spatial consistency of our reconstruction.

In general, most of the discussed summer temperature reconstructions from previous work are within the uncertainty limits of our reconstruction and several of the spatial patterns arising from the literature are reflected in our results. However, some of the coldest reported anomalies are outside of our uncertainty estimates. This is perhaps due to the smoothing effect of the spatial interpolation which leads to a less heterogeneous reconstruction compared to considering only individual records.

Our consistently inferred dryer conditions during the LGM in Siberia are in agreement with previous work (e.g. Tarasov et al., 1999; Sher et al., 2005; Pitul'Ko et al., 2007; Lozhkin et al., 2007; Andreev et al., 2011; Ashastina et al., 2018). However, some of the studies like Tarasov et al. (1999) reconstruct an even stronger reduction of precipitation. We only estimate precipitation similar to present-day for parts of the Pacific sector. Based on indirect glacier modeling, Meyer and Barr (2017) suggest similar or higher precipitation amounts during the LGM for the Kamchatka peninsula. However, for this part of the Pacific sector we still infer reduced precipitation. This conflict might stem from uncertainties in the glacier modeling-based precipitation estimates or an underestimation of the transport of moist pacific air masses by the PMIP3 simulations, which we employ.

5.3 Potential applications and extensions

Based on our results, we find that the data-constrained state estimate is likely a better basis for analyses of large-scale features of LGM climate compared to analyzing just individual proxy records or to using only simulations. If a spatial reconstruction of the desired variable is not feasible due to missing direct proxy data (e.g. for wind speed anomalies), our results suggest to use simulations, which score comparatively well against reconstructions of potentially related variables such as temperature and precipitation. Furthermore, our results indicate that a weighted mean of ensemble members is preferable compared to the standard ensemble mean, which is more likely to be disturbed by strongly biased ensemble members in ensembles with very large spreads such as the PMIP3 LGM ensemble.

It is well-established in numerical weather prediction and historical climatology that ensemble means tend to perform better than individual ensemble members under the assumption of independent and identically distributed (iid) ensemble members (Krishnamurti et al., 1999). However, it is unclear whether this is still true in paleoclimatology. Our results indicate the opposite perhaps due to stronger large-scale biases compared to historical simulations, which might make results based on iid assumptions invalid. Meanwhile, a simple "superensemble" (Krishnamurti et al., 1999) approach, i.e. a multi-model mean that is weighted according to its fit with paleoclimate data, performs similar to the best ensemble members.

We want to highlight three possible applications of our spatial reconstructions and the ensemble member evaluations. The physical mechanisms behind the absence of a large terrestrial Siberian ice sheet during the LGM are still an open question. MTWA and P_{ANN} are important variables as they are major controls of the energy balance of glaciers (Reeh, 1989). While very low P_{ANN} values are the prevalent explanation for missing large ice sheets during the LGM in Western and Central Siberia (Stauch and Gualtieri, 2008), relatively warm summer temperatures were proposed as limiting factors for the extent of glaciers in the pacific sector (Meyer and Barr, 2017). Forcing ice sheet models with our data-constrained estimates or with weighted means of simulation ensembles might result in new insights into the mechanisms behind the glacial history of Siberia.

A large amount of carbon is stored in Siberian soils (Hugelius et al., 2014). To constrain estimates of carbon fluxes under global warming, biogeochemistry models have to be tested against past glacial-interglacial transitions. This requires precise atmospheric forcing. Current estimates of the net carbon balance between the LGM and today are diverging, with Zech et al. (2011) diagnosing a large storage of carbon in LGM permafrost soils, whereas the data-based estimate of Lindgren et al. (2018) and the model-based estimate of Jeltsch-Thömmes et al. (2019) infer lower carbon storage during the LGM.

Reconciling data- and model-based estimates could be feasible by reducing biases from using single climate simulations as atmospheric forcings and by instead employing data-constrained state estimates.

Siberia has been identified as a potential area for large-scale carbon storage through afforestation (Bastin et al., 2019). To improve model-based estimates of afforestation rates our spatial reconstruction can be used to force vegetation models as a test of their ability to model the afforestation between the LGM and today.

The uncertainty estimates of the reconstruction (see Sect. 4.2) and the cross-validation experiments (see Online Resource 1) indicate where new data can clearly improve existing state estimates. The large MTWA uncertainties in Western Siberia between Ob and Lena due to missing proxy constraints and a large PMIP3 ensemble spread indicate that new data in these regions could sharpen our MTWA reconstructions the most. The cross-validation experiments show distinct negative skill at the location of the westernmost proxy sample. More data in this region would help to inspect whether this sample is an outlier or whether model biases need to be overcome in this region. A key issue remains that the uncertainty for P_{ANN} in the pollen-based reconstructions is very high, hence reducing its impact on the state estimate. Here, adding constraints from other aridity-recording proxies like ice wedges, macrofossils, or faunal remains would improve the estimates the most.

Since these archives are also interpreted as proxies for winter temperature, MTCO could be added as third climate variable to our state estimates if a sufficient spatial proxy coverage is obtained. This would additionally allow to better constraint T_{ANN} which is not possible from the MTWA reconstruction alone.

6 Conclusions

We present new LGM climate reconstructions from an extensive compilation of Siberian pollen records. WAPLS transfer functions are used to compute local reconstruction of MTWA and P_{ANN} for large parts of Siberia. The reconstructions feature mostly colder temperatures and less precipitation. However, several records along the modern coastlines show temperatures near modern values and in the Amur region slightly more precipitation than present-day is reconstructed. While reconstructions are predominantly consistent on local-to-regional scales, the anomalies from individual records are rarely statistically significant.

We combine the local reconstructions with an ensemble of model simulations for the LGM and compute spatial reconstructions of MTWA and P_{ANN}. The reconstruction framework performs well in cross-validation and pseudo-proxy experiments. It provides a data-constrained state estimate which adjusts the ensemble mean according to the proxy data and reduces the uncertainty in the unconstrained PMIP3 ensemble. While our estimates are cooler than the modern climate with less precipitation in all areas except for some coastal regions and the Siberian shelf, the spatial reconstructions are warmer and wetter than the PMIP3 ensemble mean.

By computing the LLS of each ensemble member, we quantify the fit of proxy data and climate simulations. The comparison reveals that simulations with a relatively warm and wet LGM in Siberia perform mostly better, although mismatching medium-to-large scale patterns can diminish the performance. The higher scoring models tend to have a smaller Northern Hemisphere polar amplification, a less enhanced polar jet stream, and just a slighty negative geopotential anomaly compared to the ensemble mean. Our results indicate that while the Siberian atmospheric state was altered during the LGM in response to the large Fennoscandian ice sheet, lower CO_2 levels, lower sea levels, and varied insolation patterns, the changes during the Siberian summer were less extreme than in several PMIP3 simulations.

Author contributions

Nils Weitzel, Ulrike Herzschuh, Andreas Hense, and Kira Rehfeld designed the study. Xianyong Cao and Thomas Böhmer computed the local reconstructions. Nils Weitzel implemented the spatial reconstruction and model evaluation framework. All authors discussed the results. Nils Weitzel wrote the first version of the manuscript and all authors commented on previous versions of the manuscript. All authors read and approved the final manuscript.

Acknowledgements

NW and KR acknowledge funding by the German Research Foundation (DFG, code RE3994-2/1) and the Heidelberg Center for the Environment for providing a venue for discussion. NW was additionally supported by the German Federal Ministry of Education and Research (BMBF) as Research for Sustainability initiative (FONA) through the PalMod project (FKZ: 01LP1509D). TB and UH acknowledge support from the Helmholtz Gemeinschaft and H2020 European Research Council project Glacial Legacy (Grant Number: 772852), and from the German Federal Ministry of Education and Research (BMBF) through the PalMod project (FKZ: 01LP1923B).

We thank Thomas Opel, Florian Kapp, and Christian Ohlwein for insightful discussions and comments on previous versions of the manuscript. We acknowledge all groups involved in producing and making available the PMIP3 multi-model ensemble. We acknowledge the World Climate Research Programme's Working Group on Coupled Modelling, which is responsible for CMIP. We acknowledge all palynologists who, either directly or indirectly, contributed their pollen records to the pollen dataset or accessible databases.

Code for computing the spatial reconstructions is available at `https://bitbucket.org/nils_weitzel/spatial_reconstr_repo`. Data and code for reproducing the figures of the manuscript will be made available on Figshare upon acceptance of the manuscript.

Conflict of interest

The authors declare that they have no conflict of interest.

7 References

Abe-Ouchi, A., Saito, F., Kageyama, M., Braconnot, P., Harrison, S. P., Lambeck, K., Otto-Bliesner, B. L., Peltier, W. R., Tarasov, L., Peterschmitt, J. Y., and Takahashi, K.: Ice-sheet configuration in the CMIP5/PMIP3 Last Glacial Maximum experiments, Geoscientific Model Development, 8, 3621–3637, https://doi.org/10.5194/gmd-8-3621-2015, 2015.

Alfimov, A. V. and Berman, D. I.: Beringian climate during the Late Pleistocene and Holocene, Quaternary Science Reviews, 20, 127–134, https://doi.org/10.1016/S0277-3791(00)00128-1, 2001.

Andreev, A. A., Schirrmeister, L., Tarasov, P. E., Ganopolski, A., Brovkin, V., Siegert, C., Wetterich, S., and Hubberten, H. W.: Vegetation and climate history in the Laptev Sea region (Arctic Siberia) during Late Quaternary inferred from pollen records, Quaternary Science Reviews, 30, 2182–2199, https://doi.org/10.1016/j.quascirev.2010.12.026, 2011.

Annan, J. D. and Hargreaves, J. C.: A new global reconstruction of temperature changes at the Last Glacial Maximum, Climate of the Past, 9, 367–376, https://doi.org/10.5194/cp-9-367-2013, 2013.

Ashastina, K., Kuzmina, S., Rudaya, N., Troeva, E., Schoch, W. H., Römermann, C., Reinecke, J., Otte, V., Savvinov, G., Wesche, K., and Kienast, F.: Woodlands and steppes: Pleistocene vegetation in Yakutia's most continental part recorded in the Batagay permafrost sequence, Quaternary Science Reviews, 196, 38–61, https://doi.org/10.1016/j.quascirev.2018.07.032, 2018.

Bartlein, P. J., Harrison, S. P., Brewer, S., Connor, S., Davis, B. A. S., Gajewski, K., Guiot, J., Harrison-Prentice, T. I., Henderson, A., Peyron, O., Prentice, I. C., Scholze, M., Seppä, H., Shuman, B., Sugita, S., Thompson, R. S., Viau, A. E., Williams, J., and Wu, H.: Pollen-based continental climate reconstructions at 6 and 21 ka: a global synthesis, Climate Dynamics, 37, 775–802, https://doi.org/10.1007/s00382-010-0904-1, 2011.

Bastin, J.-F., Finegold, Y., Garcia, C., Mollicone, D., Rezende, M., Routh, D., Zohner, C. M., and Crowther, T. W.: The global tree restoration potential, Science, 365, 76–79, https://doi.org/10.1126/science.aax0848, 2019.

Batchelor, C. L., Margold, M., Krapp, M., Murton, D. K., Dalton, A. S., Gibbard, P. L., Stokes, C. R., Murton, J. B., and Manica, A.: The configuration of Northern Hemisphere ice sheets through the Quaternary, Nature Communications, 10, 1–10, https://doi.org/10.1038/s41467-019-11601-2, 2019.

Berman, D., Alfimov, A., and Kuzmina, S.: Invertebrates of the relict steppe ecosystems of Beringia, and the reconstruction of Pleistocene landscapes, Quaternary Science Reviews, 30, 2200–2219, https://doi.org/10.1016/j.quascirev.2010.09.016, 2011.

Birks, H. J. B., Heiri, O., Seppä, H., and Bjune, A. E.: Strengths and Weaknesses of Quantitative Climate Reconstructions Based on Late-Quaternary Biological Proxies, The Open Ecology Journal, 3, 68–110, https://doi.org/10.2174/1874213001003020068, 2010.

Blaauw, M. and Christen, J. A.: Flexible Paleoclimate Age-Depth Models Using an Autoregressive Gamma Process, Bayesian Analysis, 6, 457–474, https://doi.org/10.1214/11-BA618, 2011.

Braconnot, P., Harrison, S. P., Otto-Bliesner, B., Abe-Ouchi, A., Jungclaus, J., and Peterschmitt, J.-Y.: The Paleoclimate Modeling Intercomparison Project contribution to CMIP5, CLIVAR Exchanges, 56/16/2, 15–19, 2011.

Braconnot, P., Harrison, S. P., Kageyama, M., Bartlein, P. J., Masson-Delmotte, V., Abe-Ouchi, A., Otto-Bliesner, B., and Zhao, Y.: Evaluation of climate models using palaeoclimatic data, Nature Climate Change, 2, 417–424, https://doi.org/10.1038/NCLIMATE1456, 2012.

Cao, X., Ni, J., Herzschuh, U., Wang, Y.-b., and Zhao, Y.: A late Quaternary pollen dataset from eastern continental Asia for vegetation and climate reconstructions: Set up and evaluation, Review of Palaeobotany and Palynology, 194, 21–37, https://doi.org/10.1016/j.revpalbo.2013.02.003, 2013.

Cao, X., Herzschuh, U., Telford, R., and Ni, J.: A modern pollen-climate dataset from China and Mongolia: Assessing its potential for climate reconstructions, Review of Palaeobotany and Palynology, 211, 87–96, https://doi.org/10.1016/j.revpalbo.2014.08.007, 2014.

Cao, X., Tian, F., Andreev, A., Anderson, P. M., Lozhkin, A. V., Bezrukova, E., Ni, J., Rudaya, N., Stobbe, A., Wieczorek, M., and Herzschuh, U.: A taxonomically harmonized and temporally standardized fossil pollen dataset from Siberia covering the last 40 kyr, Earth System Science Data, 12, 119–135, https://doi.org/10.5194/essd-12-119-2020, 2020.

Cleator, S. F., Harrison, S. P., Nichols, N. K., Prentice, I. C., and Roulstone, I.: A method for generating coherent spatially explicit maps of seasonal palaeoclimates from sitebased reconstructions, Journal of Advances in Modeling Earth Systems, 12, https://doi.org/10.1029/2019MS001630, 2019.

Colman, S. M., Peck, J. A., Karabanov, E. B., Carter, S. J., Bradbury, J. P., King, J. W., and Williams, D. F.: Continental climate response to orbital forcing from biogenic silica records in lake baikal, Nature, 378, 769–771, https://doi.org/10.1038/378769a0, 1995.

Compo, G. P., Whitaker, J. S., Sardeshmukh, P. D., Matsui, N., Allan, R. J., Yin, X., Gleason, B. E., Vose, R. S., Rutledge, G., Bessemoulin, P., BroNnimann, S., Brunet, M., Crouthamel, R. I., Grant, A. N., Groisman, P. Y., Jones, P. D., Kruk, M. C., Kruger, A. C., Marshall, G. J., Maugeri, M., Mok, H. Y., Nordli, O., Ross, T. F., Trigo, R. M., Wang, X. L., Woodruff, S. D., and Worley, S. J.: The Twentieth Century Reanalysis Project, Quarterly Journal of the Royal Meteorological Society, 137, 1–28, https://doi.org/10.1002/qj.776, 2011.

Dorofeeva, R. P., Shen, P. Y., and Shapova, M. V.: Ground surface temperature histories inferred from deep borehole temperature-depth data in Eastern Siberia, Earth and Planetary Science Letters, 203, 1059–1071, https://doi.org/10.1016/S0012-821X(02)00925-1, 2002.

Gneiting, T. and Raftery, A. E.: Strictly Proper Scoring Rules, Prediction, and Estimation, Journal of the American Statistical Association, 102/477, 359–378, https://doi.org/10.1198/016214506000001437, 2007.

Gong, D. Y. and Ho, C. H.: The Siberian High and climate change over middle to high latitude Asia, Theoretical and Applied Climatology, 72, 1–9, https://doi.org/10.1007/s007040200008, 2002.

Hugelius, G., Strauss, J., Zubrzycki, S., Harden, J. W., Schuur, E. A., Ping, C. L., Schirrmeister, L., Grosse, G., Michaelson, G. J., Koven, C. D., O'Donnell, J. A., Elberling, B., Mishra, U., Camill, P., Yu, Z., Palmtag, J., and Kuhry, P.: Estimated stocks of circumpolar permafrost carbon with quantified uncertainty ranges and identified data gaps, Biogeosciences, 11, 6573–6593, https://doi.org/10.5194/bg-11-6573-2014, 2014.

Hughes, A. L. C., Gyllencreutz, R., Lohne, O. S., Mangerud, J., and Svendsen, J. I.: The last Eurasian ice sheets - a chronological database and time-slice reconstruction, DATED-1, Boreas, 45, 1–45, https://doi.org/10.1111/bor.12142, 2015.

Hughes, P. D., Gibbard, P. L., and Ehlers, J.: Timing of glaciation during the last glacial cycle: Evaluating the concept of a global 'Last Glacial Maximum' (LGM), Earth-Science Reviews, 125, 171–198, https://doi.org/10.1016/j.earscirev.2013.07.003, 2013.

Jeltsch-Thömmes, A., Battaglia, G., Cartapanis, O., Jaccard, S. L., and Joos, F.: Low terrestrial carbon storage at the Last Glacial Maximum: Constraints from multi-proxy data, Climate of the Past, 15, 849–879, https://doi.org/10.5194/cp-15-849-2019, 2019.

Juggins, S.: Quantitative reconstructions in palaeolimnology: new paradigm or sick science?, Quaternary Science Reviews, 64, 20–32, https://doi.org/10.1016/j.quascirev.2012.12.014, 2013.

Juggins, S.: rioja: Analysis of Quaternary Science Data, R package version 0.9-21, URL `http://www.staff.ncl.ac.uk/stephen.juggins/`, 2017.

Juggins, S. and Birks, H. J. B.: Quantitative Environmental Reconstructions from Biological Data, pp. 431–494, Springer Netherlands, Dordrecht, https://doi.org/10.1007/978-94-007-2745-8_14, 2012.

Kageyama, M., Albani, S., Braconnot, P., Harrison, S. P., Hopcroft, P. O., Ivanovic, R. F., Lambert, F., Marti, O., Peltier, W. R., Peterschmitt, J.-Y., Roche, D. M., Tarasov, L., Zhang, X., Brady, E. C., Haywood, A. M., LeGrande, A. N., Lunt, D. J., Mahowald, N. M., Mikolajewicz, U., Nisancioglu, K. H., Otto-Bliesner, B. L., Renssen, H., Tomas, R. A., Zhang, Q., Abe-Ouchi, A., Bartlein, P. J., Cao, J., Li, Q., Lohmann, G., Ohgaito, R., Shi, X., Volodin, E., Yoshida, K., Zhang, X., and Zheng, W.: The PMIP4 contribution to CMIP6 – Part 4: Scientific objectives and experimental design of the PMIP4-CMIP6 Last Glacial Maximum experiments and PMIP4 sensitivity experiments, Geoscientific Model Development, 10, 4035–4055, https://doi.org/10.5194/gmd-10-4035-2017, 2017.

Karger, D. N., Conrad, O., Böhner, J., Kawohl, T., Kreft, H., Soria-Auza, R. W., Zimmermann, N. E., Linder, H. P., and Kessler, M.: Climatologies at high resolution for the earth's land surface areas, Scientific Data, 4, 1–20, https://doi.org/10.1038/sdata.2017.122, 2017.

Kiefer, T., Sarnthein, M., Erlenkeuser, H., Grootes, P. M., and Roberts, A. P.: North Pacific response to millennial-scale changes in ocean circulation over the last 60 kyr, Paleoceanography, 16, 179–189, https://doi.org/10.1029/2000PA000545, 2001.

Kienast, F., Schirrmeister, L., Siegert, C., and Tarasov, P.: Palaeobotanical evidence for warm summers in the East Siberian Arctic during the last cold stage, Quaternary Research, 63, 283–300, https://doi.org/10.1016/j.yqres.2005.01.003, 2005.

Köhler, P., Nehrbass-Ahles, C., Schmitt, J., Stocker, T. F., and Fischer, H.: A 156 kyr smoothed history of the atmospheric greenhouse gases CO2, CH4, and N2O and their radiative forcing, Earth System Science Data, 9, 363–387, https://doi.org/10.5194/essd-9-363-2017, 2017.

Krishnamurti, T. N., Kishtawal, C. M., LaRow, T. E., Bachiochi, D. R., Zhang, Z., Williford, C. E., Gadgil, S., and Surendran, S.: Improved Weather and Seasonal Climate Forecasts from Multimodel Superensemble, Science, 285, 1548–1550, https://doi.org/10.1126/science.285.5433.1548, 1999.

Lambeck, K., Rouby, H., Purcell, A., Sun, Y., and Sambridge, M.: Sea level and global ice volumes from the Last Glacial Maximum to the Holocene, Proceedings of the National Academy of Sciences, 111, 15 296–15 303, https://doi.org/10.1073/pnas.1411762111, 2014.

Lindgren, A., Hugelius, G., and Kuhry, P.: Extensive loss of past permafrost carbon but a net accumulation into present-day soils, Nature, 560, 219–222, https://doi.org/10.1038/s41586-018-0371-0, 2018.

Löfverström, M., Caballero, R., Nilsson, J., and Kleman, J.: Evolution of the large-scale atmospheric circulation in response to changing ice sheets over the last glacial cycle, Climate of the Past, 10, 1453–1471, https://doi.org/10.5194/cp-10-1453-2014, 2014.

Lozhkin, A. V., Anderson, P. M., Matrosova, T. V., and Minyuk, P. S.: The pollen record from El'gygytgyn Lake: Implications for vegetation and climate histories of northern Chukotka since the late middle Pleistocene, Journal of Paleolimnology, 37, 135–153, https://doi.org/10.1007/s10933-006-9018-5, 2007.

MARGO Project Members: Constraints on the magnitude and patterns of ocean cooling at the Last Glacial Maximum, Nature Geoscience, 2, 127–132, https://doi.org/10.1038/ngeo411, 2009.

Masson-Delmotte, V., Kageyama, M., Braconnot, P., Charbit, S., Krinner, G., Ritz, C., Guilyardi, E., Jouzel, J., Abe-Ouchi, A., Crucifix, M., Gladstone, R. M., Hewitt, C. D., Kitoh, A., LeGrande, A. N., Marti, O., Merkel, U., Motoi, T., Ohgaito, R., Otto-Bliesner, B., Peltier, W. R., Ross, I., Valdes, P. J., Vettoretti, G., Weber, S. L., Wolk, F., and Yu, Y.: Past and future polar amplification of climate change: Climate model intercomparisons and ice-core constraints, Climate Dynamics, 26, 513–529, https://doi.org/10.1007/s00382-005-0081-9, 2006.

Meyer, H., Dereviagin, A., Siegert, C., Schirrmeister, L., and Hubberten, H. W.: Palaeoclimate reconstruction on Big Lyakhovsky Island, North Siberia - Hydrogen and oxygen isotopes in ice wedges, Permafrost and Periglacial Processes, 13, 91–105, https://doi.org/10.1002/ppp.416, 2002.

Meyer, V. and Barr, I.: Linking glacier extent and summer temperature in NE Russia - Implications for precipitation during the global Last Glacial Maximum, Palaeogeography, Palaeoclimatology, Palaeoecology, 470, 72–80, https://doi.org/10.1016/j.palaeo.2016.12.038, 2017.

Meyer, V. D., Max, L., Hefter, J., Tiedemann, R., and Mollenhauer, G.: Glacial-to-Holocene evolution of sea surface temperature and surface circulation in the subarctic northwest Pacific and the Western Bering Sea, Paleoceanography, 31, 916–927, https://doi.org/10.1002/2015PA002877, 2016.

Meyer, V. D., Hefter, J., Lohmann, G., Max, L., Tiedemann, R., and Mollenhauer, G.: Summer temperature evolution on the Kamchatka Peninsula, Russian Far East, during the past 20 000 years, Climate of the Past, 13, 359–377, https://doi.org/10.5194/cp-13-359-2017, 2017.

Miao, C., Duan, Q., Sun, Q., Huang, Y., Kong, D., Yang, T., Ye, A., Di, Z., and Gong, W.: Assessment of CMIP5 climate models and projected temperature changes over Northern Eurasia, Environmental Research Letters, 9, https://doi.org/10.1088/1748-9326/9/5/055007, 2014.

Mock, C. J., Bartlein, P. J., and Anderson, P. M.: Atmospheric circulation patterns and spatial climatic variations in Beringia, International Journal of Climatology, 18, 1085–1104, https://doi.org/10.1002/(SICI)1097-0088(199808)18:10⟨1085::AID-JOC305⟩3.0.CO;2-K, 1998.

Opel, T., Murton, J. B., Wetterich, S., Meyer, H., Ashastina, K., Günther, F., Grotheer, H., Mollenhauer, G., Danilov, P. P., Boeskorov, V., Savvinov, G. N., and Schirrmeister, L.: Past climate and continentality inferred from ice wedges at Batagay megaslump in the Northern Hemisphere's most continental region, Yana Highlands, interior Yakutia, Climate of the Past, 15, 1443–1461, https://doi.org/10.5194/cp-15-1443-2019, 2019.

Otto-Bliesner, B. L., Brady, E. C., Clauzet, G., Tomas, R., Levis, S., and Kothavala, Z.: Last glacial maximum and Holocene climate in CCSM3, Journal of Climate, 19, 2526–2544, https://doi.org/10.1175/JCLI3748.1, 2006.

Pitul'Ko, V. V., Pavlova, E. Y., Kuz'Mina, S. A., Nikol'Skii, P. A., Basilyan, A. E., Tumskoi, V. E., and Anisimov, M. A.: Natural-climatic changes in the Yana-Indigirka lowland during the terminal Kargino time and habitat of late Paleolithic man in northern part of East Siberia, Doklady Earth Sciences, 417, 1256–1260, https://doi.org/10.1134/S1028334X07080284, 2007.

Reeh, N.: Parameterization of Melt Rate and Surface Temperature on the Greenland lce Sheet, Polarforschung, 59, 113–128, 1989.

Rehfeld, K., Trachsel, M., Telford, R. J., and Laepple, T.: Assessing performance and seasonal bias of pollen-based climate reconstructions in a perfect model world, Climate of the Past, 12, 2255–2270, https://doi.org/10.5194/cp-12-2255-2016, 2016.

Rohde, R., Muller, R. A., Jacobsen, R., Muller, E., Perlmutter, S., Rosenfeld, A., Wurtele, J., Groom, D., and Wickham, C.: A New Estimate of the Average Earth Surface Land Temperature Spanning 1753 to 2011, Geoinformatics & Geostatistics: An Overview, 01, 1–7, https://doi.org/10.4172/2327-4581.1000101, 2013.

Seki, O., Sakamoto, T., Sakai, S., Schouten, S., Hopmans, E. C., Damste, J. S., and Pancost, R. D.: Large changes in seasonal sea ice distribution and productivity in the Sea of Okhotsk during the deglaciations, Geochemistry, Geophysics, Geosystems, 10, 1–10, https://doi.org/10.1029/2009GC002613, 2009.

Sher, A. V., Kuzmina, S. A., Kuznetsova, T. V., and Sulerzhitsky, L. D.: New insights into the Weichselian environment and climate of the East Siberian Arctic, derived from fossil insects, plants, and mammals, Quaternary Science Reviews, 24, 533–569, https://doi.org/10.1016/j.quascirev.2004.09.007, 2005.

Stauch, G. and Gualtieri, L.: Late Quaternary glaciations in northeastern Russia, Journal of Quaternary Science, 23, 545–558, https://doi.org/10.1002/jqs.1211, 2008.

Svendsen, J. I., Alexanderson, H., Astakhov, V. I., Demidov, I., Dowdeswell, J. A., Funder, S., Gataullin, V., Henriksen, M., Hjort, C., Houmark-Nielsen, M., Hubberten, H. W., Ingólfsson, Ó., Jakobsson, M., Kjær, K. H., Larsen, E., Lokrantz, H., Lunkka, J. P., Lyså, A., Mangerud, J., Matiouchkov, A., Murray, A., Möller, P., Niessen, F., Nikolskaya, O., Polyak, L., Saarnisto, M., Siegert, C., Siegert, M. J., Spielhagen, R. F., and Stein, R.: Late Quaternary ice sheet history of northern Eurasia, Quaternary Science Reviews, 23, 1229–1271, https://doi.org/10.1016/j.quascirev.2003.12.008, 2004.

Tarasov, P. E., Peyron, O., Guiot, J., Brewer, S., Volkova, V. S., Bezusko, L. G., Dorofeyuk, N. I., Kvavadze, E. V., Osipova, I. M., and Panova, N. K.: Last Glacial Maximum climate of the former Soviet Union and Mongolia reconstructed from pollen and plant macrofossil data, Climate Dynamics, 15, 227–240, https://doi.org/10.1007/s003820050278, 1999.

Telford, R. J. and Birks, H. J.: A novel method for assessing the statistical significance of quantitative reconstructions inferred from biotic assemblages, Quaternary Science Reviews, 30, 1272–1278, https://doi.org/10.1016/j.quascirev.2011.03.002, 2011.

Ter Braak, C. J. and Juggins, S.: Weighted averaging partial least squares regression (WA-PLS): an improved method for reconstructing environmental variables from species assemblages, Hydrobiologia, 269-270, 485–502, https://doi.org/10.1007/BF00028046, 1993.

Ter Braak, C. J. F., Juggins, S., Birks, H. J. B., and van der Voet, H.: Weighted averaging partial least squares regression (WA-PLS): Definition and comparison with other methods for species-environment calibration, pp. 525–560, Elsevier Science, 1993.

van der Voet, H.: Comparing the predictive accuracy of models using a simple randomization test, Chemometrics and Intelligent Laboratory Systems, 25, 313–323, https://doi.org/10.1016/0169-7439(94)85050-X, 1994.

Weitzel, N., Hense, A., and Ohlwein, C.: Combining a pollen and macrofossil synthesis with climate simulations for spatial reconstructions of European climate using Bayesian filtering, Climate of the Past, 15, 1275–1301, https://doi.org/10.5194/cp-15-1275-2019, 2019.

Wetterich, S., Rudaya, N., Tumskoy, V., Andreev, A. A., Opel, T., Schirrmeister, L., and Meyer, H.: Last Glacial Maximum records in permafrost of the East Siberian Arctic, Quaternary Science Reviews, 30, 3139–3151, https://doi.org/10.1016/j.quascirev.2011.07.020, 2011.

Williams, D. F., Peck, J., Karabanov, E. B., Prokopenko, A. A., Kravchinsky, V., King, J., and Kuzmin, M. I.: Lake Baikal record of continental climate response to orbital insolation during the past 5 million years, Science, 278, 1114–1117, https://doi.org/10.1126/science.278.5340.1114, 1997.

Zech, R., Huang, Y., Zech, M., Tarozo, R., and Zech, W.: High carbon sequestration in Siberian permafrost loess-paleosols during glacials, Climate of the Past, 7, 501–509, https://doi.org/10.5194/cp-7-501-2011, 2011.

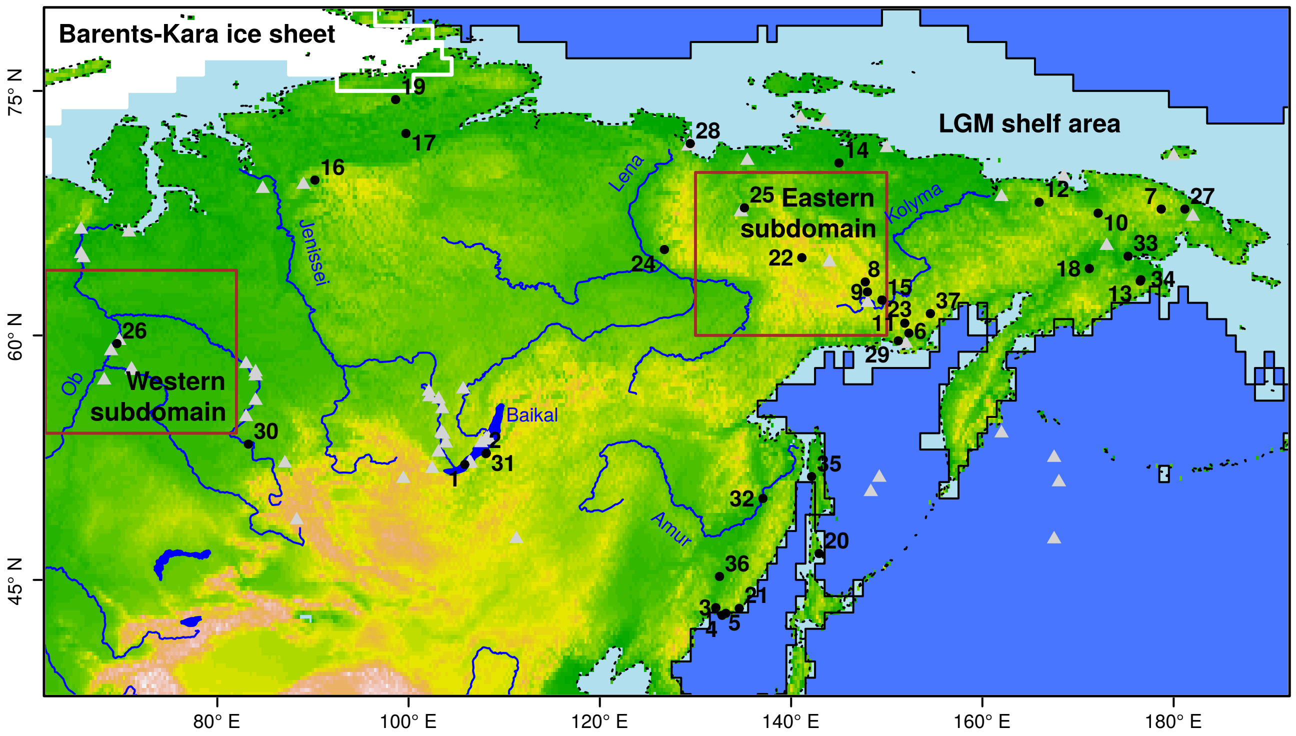

Figure 1: Spatial domain of this study. Pollen records included in the spatial reconstruction are marked by black dots. Other records mentioned in the manuscript are depicted by gray triangles. The LGM coastline is denoted by thick black lines, the modern coastline by dotted lines, the Siberian shelf by shaded blue surfaces, and the PMIP3 LGM ice sheet extent in the northwestern part of the domain by white surfaces and white lines. The two brown rectangles denote the eastern and western subdomains that are further studied in Sect. 4.2 and Fig. 5.

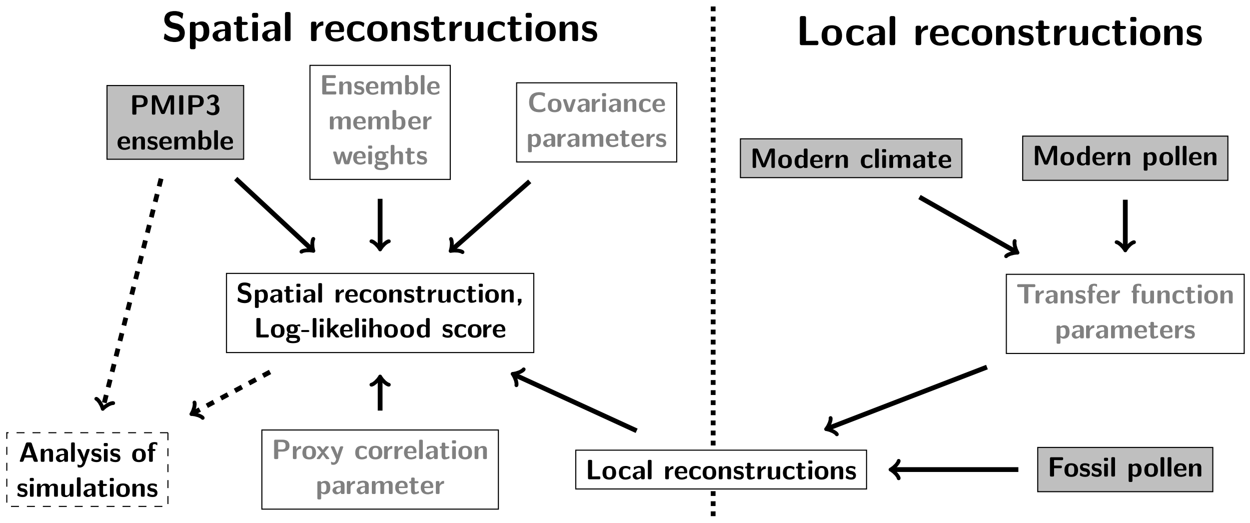

Figure 2: Graph of the workflow for local reconstructions (right hand side), spatial reconstructions, and model evaluation (left hand side). Involved quantities are given by nodes. Nodes with gray background denote input data and nodes with gray font are statistical model parameters. Arrows indicate contributions to the output products.

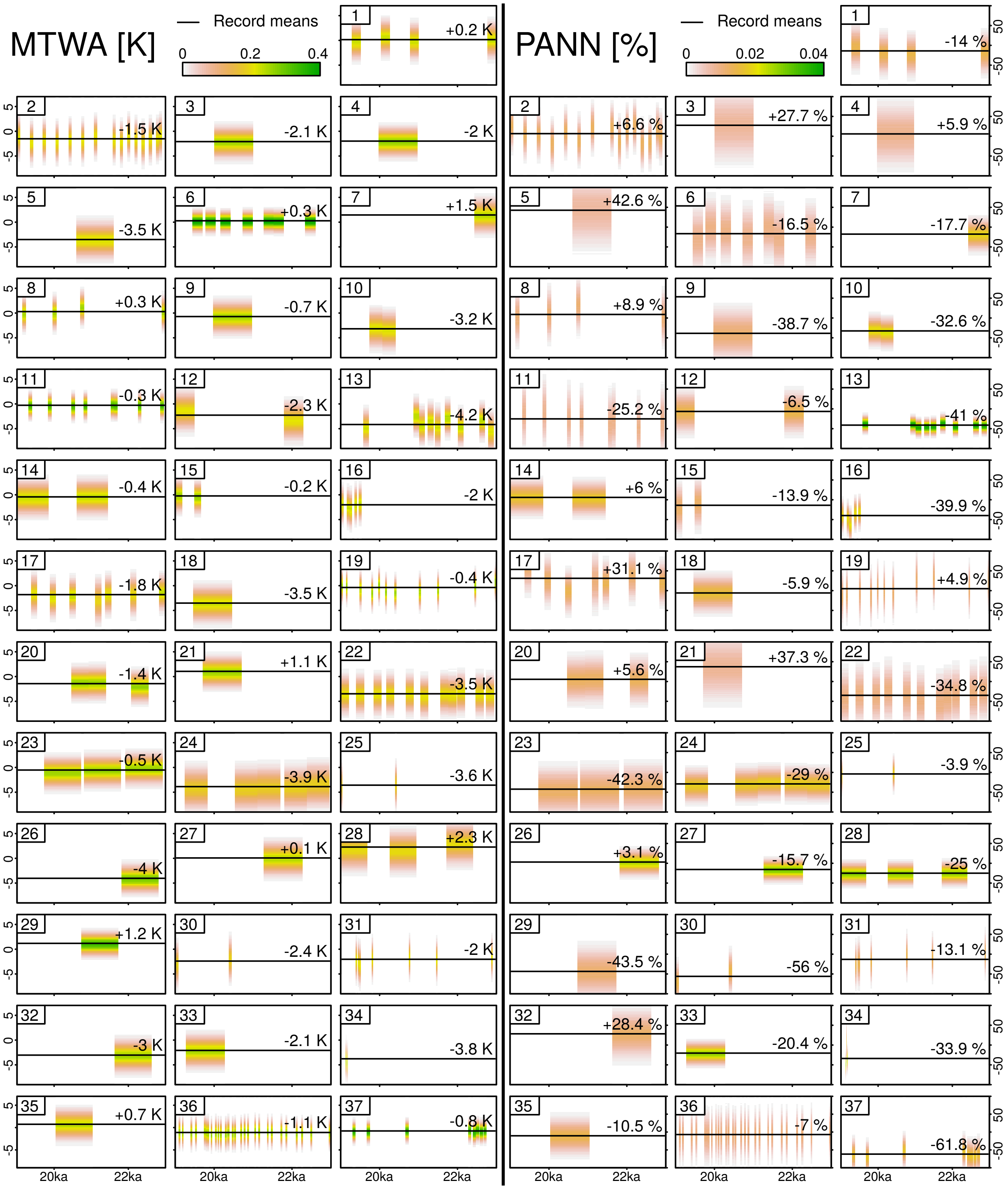

Figure 3: Local MTWA and P_{ANN} climate reconstructions with WAPLS transfer functions. The indices of the records correspond to the locations in Fig. 1. Reconstruction uncertainties are quantified by probability densities, which are depicted by colored bars. Black lines denote the sample means of the records.

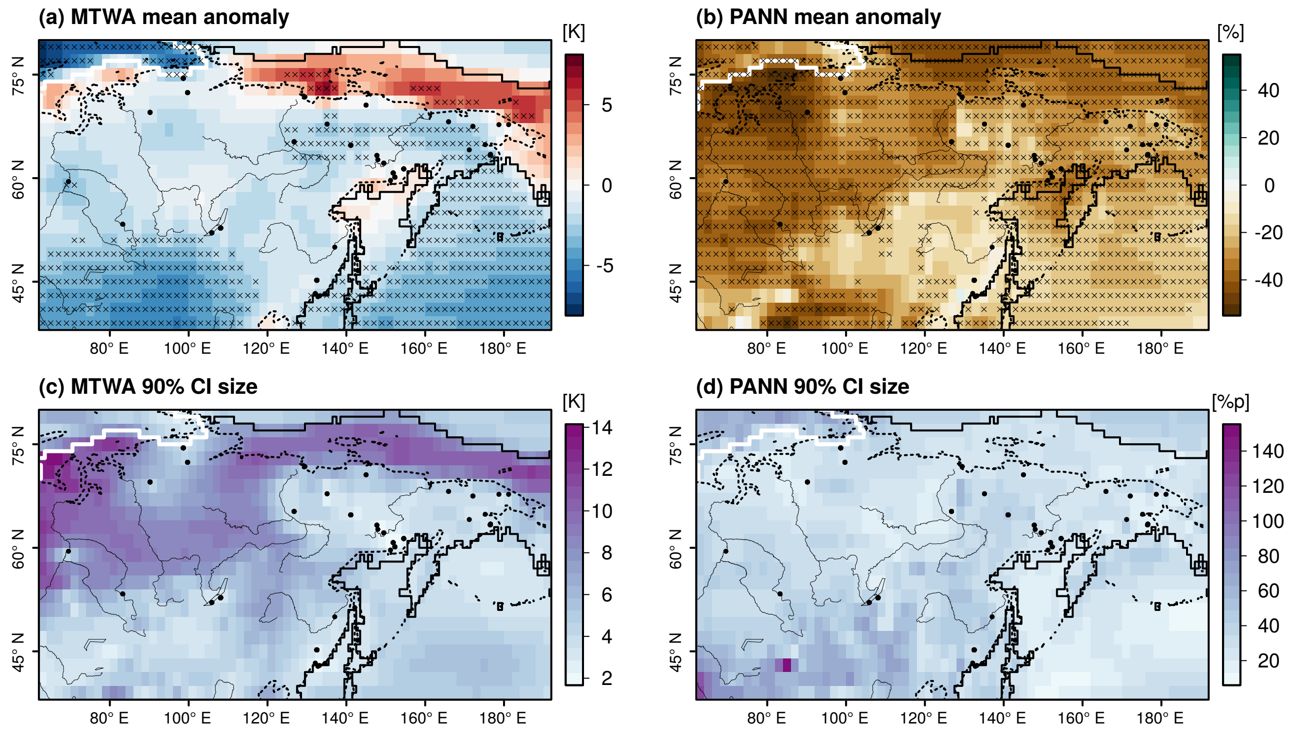

Figure 4: Spatial reconstruction of MTWA and P_{ANN}. (a) MTWA posterior mean anomaly, (b) P_{ANN} posterior mean anomaly, (c) MTWA reconstruction uncertainty quantified by the size of grid box-wise 90% CIs, (d) size of P_{ANN} 90% CIs. Black dots depict proxy records. In the top row, grid box-wise significant anomalies ($p \leq 0.05$) are marked by black crosses. The LGM coastline is denoted by thick black lines, the modern coastline by dotted lines, major rivers by thin black lines, and the PMIP3 LGM ice sheet extent in the northwestern part of the domain by a white line.

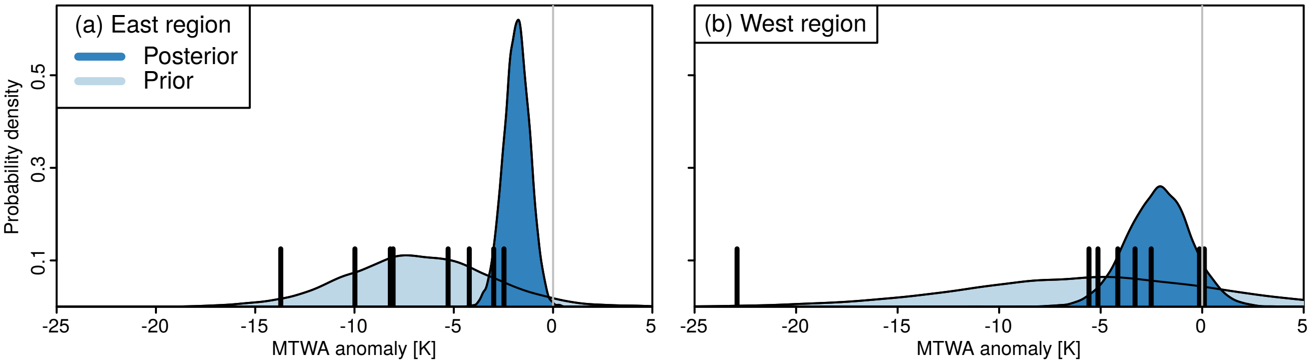

Figure 5: Effect of the proxy data on the unconstrained PMIP3 ensemble. Posterior (dark blue) and prior (light blue) probability densities of MTWA averages in the (a) eastern and (b) western subdomains. The black bars denote anomalies of the ensemble members. The prior quantifies the uncertainty in the PMIP3 ensemble due to inter-model differences and small ensemble size. The eastern region is better covered by proxy data leading to more precise posterior estimates, while the western region is strongly affected by one ensemble member outlier. See Fig.1 for the area definition.

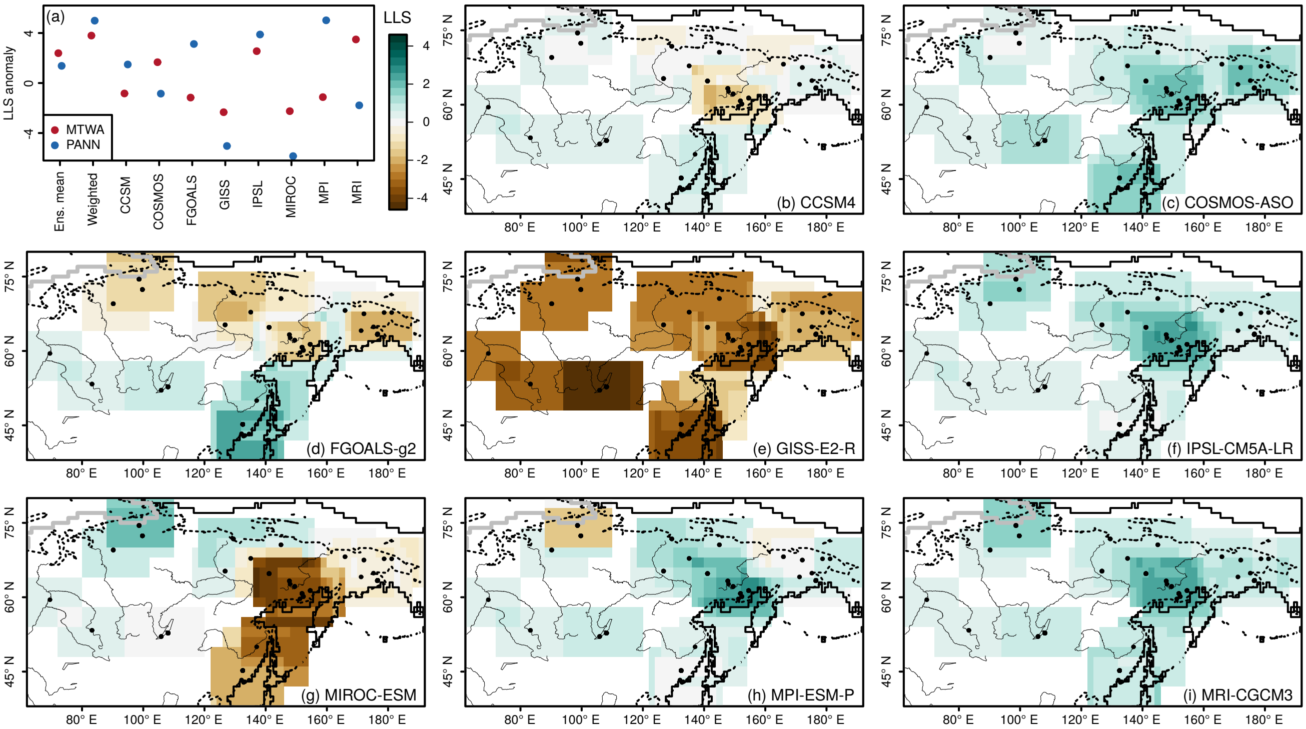

Figure 6: LLS anomalies from the mean of the ensemble mean scores. (a) Whole domain LLS anomaly for MTWA and P_{ANN} of the individual ensemble members, the ensemble mean, and a weighted mean with weights according to the ensemble member likelihoods. (b-i) Spatial distribution of regional MTWA LLS anomalies for each ensemble member by using moving windows (size 22 x 10 degree). Positive values denote a better fit with the data.

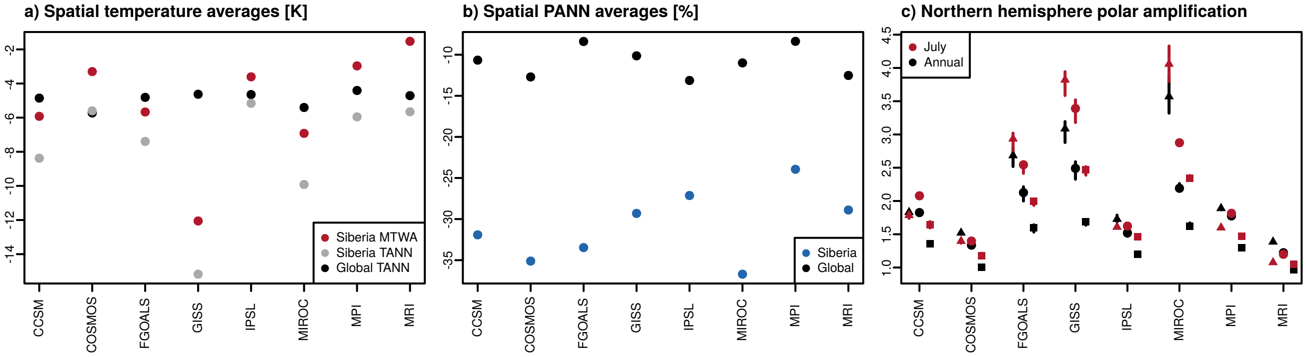

Figure 7: Comparison of large-scale properties of the ensemble members. (a) Siberian MTWA, Siberian T_{ANN}, and global T_{ANN} anomalies. (b) Siberian and global relative P_{ANN} anomalies. (c) Northern Hemisphere polar amplification at 500 hPa (triangles), 600 hPa (circles) and 700 hPa (squares) computed as the ratio of the anomalies from 70° N to 90° N and from 0° to 20° N. The uncertainty bars are computed from varying the size of the latitudinal bands by ±5°.

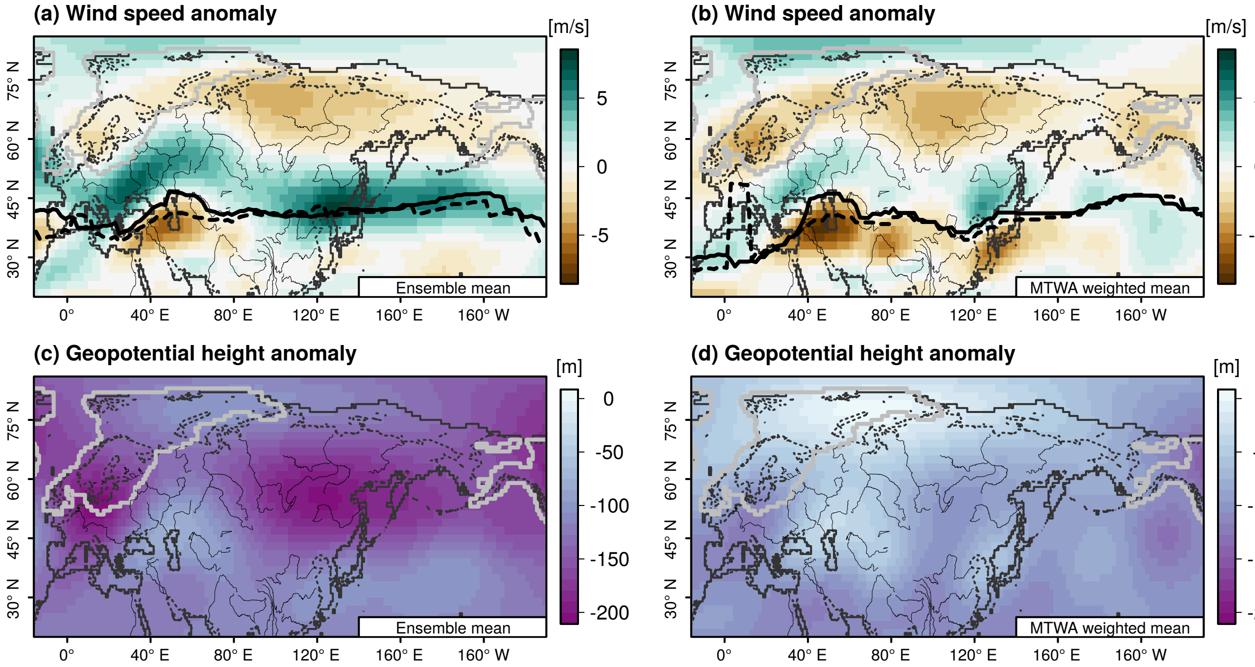

Figure 8: (a) July wind speed anomaly at 250 hPa of the ensemble mean. The thick black line denotes the position of the maximal wind speed at each longitude during the LGM. The dotted line denotes the position of maximal wind speed in the PI ensemble mean. (b) Same as (a) but for the weighted mean with weights according to the MTWA likelihoods of each ensemble member. (c) Ensemble mean anomaly of the geopotential height at the 250 hPa pressure surface. (d) Same as (c) but for the MTWA likelihood weighted mean.

Table 1: Summary measures for the Siberian LGM reconstructions of MTWA and P_{ANN}. Numbers in brackets are minima and maxima of the corresponding 90% CIs. The added value refers to the improvement in continuous ranked probability score of the posterior distribution compared to the unconstrained PMIP3 ensemble (see Online Resource 1 for details). All other quantities are explained in Sect. 4.2

Reconstruction variable	Mean anomaly	Mean 90% CI size	Uncertainty reduction	Anomaly from PMIP3 mean	Value added	Best fitting simulation	Proxy correlation	Decorrelation length
MTWA	(-1.19 K) -1.93 (-2.68 K)	5.45 K	58.4%	+3.3 K	62.0%	MRI-CGCM3	(0.89) 0.91 (0.93)	31.8°
P_{ANN}	(-21.4%) -26.2% (-30.8%)	34.0 %p	8.9%	+4.6 %p	10.7%	MPI-ESM-P	(0.76) 0.80 (0.84)	6.8°

Table 2: Comparison of our reconstructions with previous work based on six subdomains. To homogenize the estimate takes from other studies, we translate them into qualitative estimates. For our reconstructions, we show the spatial mean anomaly and for MTWA in addition the 5% and 95% percentiles of all local anomalies (inlcuding uncertainty ranges). These represent local heterogeneity for a better comparison with previous local estimates. The definition of the subdomains and a rough translation of the qualitative MTWA estimates to temperature intervals are provided in Online Resource 1.

Region	Spatial mean MTWA	Local 5% percentile MTWA	Local 95% percentile MTWA	Literature estimates MTWA	Spatial mean P_{ANN}	Literature estimates P_{ANN}
Western Siberia	-1.9 K	-6.0 K	+2.6 K	Substantially colder to slightly warmer	-37.7 %	Dryer
Baikal Lake	-1.4 K	-4.1 K	+1.7 K	Moderately colder (T_{ANN})	-24.6 %	Dryer
Arctic Ocean and Yana	-0.2 K	-3.7 K	+6.6 K	Moderately colder to slightly warmer	-25.6 %	Dryer
Eastern Siberia	-0.7 K	-3.8 K	+5.2 K	Substantially colder to slightly warmer	-27.4 %	
Pacific and Kamchatka	-2.3 K	-4.6 K	-0.1 K	Moderately colder to similar temperature	-21.5 %	Similar
Sea of Okhotsk	-0.7 K	-2.9 K	+1.6 K	Moderately to slightly colder	-20.7 %	